Journal of
Materials Chemistry A

PAPER

View Article Online
View Journal | View Issue

Cite this: *J. Mater. Chem. A*, 2025, **13**, 26521

Development of a heat storage heater for hybrid electrothermal conversion and latent heat storage†

Takahiro Kawaguchi,[a] Yusuke Sato,[a] Joshua Chidiebere Mba,[a] Yuto Shimizu,[b] Kaixin Dong,[a] Melbert Jeem[a] and Takahiro Nomura*[a]

Received 28th February 2025
Accepted 7th July 2025

DOI: 10.1039/d5ta01665g

rsc.li/materials-a

Grid-scale long-duration energy storage (LDES) is essential for decarbonizing energy systems, including power and industrial heat systems. As an economically viable LDES technology, the development of an electrical thermal energy storage (ETES) system—comprising electrothermal conversion, thermal energy storage, and optional heat engines—is progressing. A key challenge in realizing ETES is the electrothermal conversion process at the several-hundred-MW scale. This study proposes a novel heat storage heater (HSH) that combines electrothermal conversion and thermal storage functions using phase change materials (PCMs). The HSH that achieves high-temperature TES using an alloy-based PCM is a novel material that has not been reported previously. The HSH design allows for GWh-scale heat storage at high density as a several-hundred-MW class electrothermal converter, using a microencapsulated PCM (MEPCM) with a ZnO coating and a Zn–30 mass% Al (Zn–30Al) core. The system exhibited electrical resistivities of at least 9.8 Ω cm due to a conductive network formed by ZnO in the MEPCM. Upon energization, the temperature exceeded the alloy's storage temperature, and a temperature plateau was observed at 470 °C due to the alloy's melting temperature (438–512 °C). This study paves the way for designing innovative electrothermal conversion systems, such as ETES systems.

Introduction

The importance of grid-scale energy storage is growing to address the variability and intermittency of large-scale variable renewable energy (VRE) sources, such as solar and wind energy.[1] According to IEA reports, the electricity sector's solar and wind power generation capacity is projected to increase from 134 GW and 114 GW in 2020 to 630 GW and 350 GW by 2050.[2] Correspondingly, the installed capacity of energy storage is expected to reach 400 times its current level by 2050.[3] In this context, various energy storage technologies, including lithium-ion batteries (LIB), redox flow batteries, thermal energy storage (TES), hydrogen storage, pumped hydro storage, and compressed air energy storage, are under development.[1,4] Similar to the optimal mix of power generation methods, an optimal combination of energy storage technologies is essential, as each technology offers specific durations and output ranges suitable for different applications.

Thermal energy storage (TES) is a promising solution as a type of long-duration energy storage (LDES). According to an annual report by the LDES Council, TES is a cost-competitive option for durations greater than 6–8 hours compared to LIB and for durations shorter than 150 hours compared to hydrogen storage.[3] In addition, TES offers a key advantage over other LDES options, such as pumped hydro and compressed air energy storage, by having no siting constraints.[5]

Systems incorporating TES, such as power-to-heat-to-power—commonly referred to as "Carnot batteries"—show significant potential for stabilizing and storing energy from variable renewable sources.[6] Carnot batteries store heat generated from electricity derived from VRE and convert the heat back into electricity on demand using heat engines.[7] This system offers unique features that are challenging to achieve with other energy storage technologies: rotation inertia, low construction costs, and integration with other heat applications.[8–10] In recent years, efforts have also focused on converting coal-fired power generation for alternative uses and integrating it with energy management systems, including district heating supply.[11–14]

Electrothermal energy storage (ETES), featuring an electric heater for electrothermal conversion, represents the simplest and most typical system configuration of Carnot batteries. From fundamental research studies[12,15–26] to demonstration projects,[27,28] the development of ETES systems is gaining momentum. However, a key barrier to the widespread adoption of ETES lies in the electrothermal conversion process. One big challenge is constructing electric heaters at the several-

---

[a] *Faculty of Engineering, Hokkaido University, Kita 13 Nishi 8, Kita-ku, Sapporo, 060-8628, Japan. E-mail: nms-tropy@eng.hokudai.ac.jp; Fax: +81 11 706 6849; Tel: +81 11 706 6842*

[b] *Graduate School of Engineering, Hokkaido University, Kita 13 Nishi 8, Kita-ku, Sapporo, 060-8628, Japan*

† Electronic supplementary information (ESI) available. See DOI: https://doi.org/10.1039/d5ta01665g

hundred-MW scale. The conventional "numbering-up" approach of connecting multiple hundred kW-class electric heaters in parallel is anticipated to be prohibitively expensive for achieving economically viable LDES. Additionally, larger-output capacity electric heaters, which can convert surplus low-cost electricity into thermal energy are more advantageous for ETES. These systems also provide greater flexibility to accommodate the variability of VREs. However, this comes with a trade-off: reduced capacity factors for the electric heaters.[26]

To address these challenges, we propose a novel heat storage heater (HSH) utilizing phase change materials (PCMs) with integrated hybrid electrothermal conversion and storage capabilities. The HSH concept enables the use of large volumes of thermal storage material for GWh-scale heat storage while functioning as a several-hundred-MW class electrothermal converter. Furthermore, latent heat storage (LHS), utilizing PCMs offers a higher heat storage density than sensible heat storage as a mature TES technology, enabling more compact designs.[29] However, materials used as electric heaters in HSHs must exhibit chemical stability when in contact with molten PCMs at elevated temperatures.

Although the term "HSH" has not been extensively used in prior studies, composite materials incorporating PCMs and electric heaters have been reported. The initial study by Chen *et al.* described the preparation of a composite material comprising paraffin PCM (melting temperature: 24 °C) embedded in a porous carbon nanotube sponge, designed to directly and effectively store heat from the sunlight and voltage from LIBs.[30] Based on this report, subsequent research has focused on preparation methods for porous carbon-based electric heaters and selecting suitable organic PCMs, for applications such as direct solar energy storage as electricity or light, or electronic and wearable devices temperature regulation.[30–134] Fig. S1† illustrates the distribution of storage temperatures in reported HSH studies,[30–134] while Table S1† provides a detailed summary of these investigations. Many storage temperatures of these composites are below 100 °C. Given an ambient temperature of around 25 °C, the electrothermal conversion causes irreversible losses of 80% or more at low storage temperatures below 100 °C, making these systems inapplicable for grid-scale or high-temperature applications like ETES. Introducing higher-temperature PCMs enables the development of HSHs better suited for ETES.

Therefore, in this study, a HSH with high-temperature PCMs is proposed for integration into ETES systems. The development of the HSH is guided by three key concepts:

(1) Use of metal alloys as PCMs: alloys are suitable PCMs with high melting temperatures and can store high-temperature heat. Additionally, metal alloy PCMs exhibit high thermal conductivity and provide high thermal response during heat storage and release.

(2) Use of microencapsulated PCM (MEPCM) with ZnO coating: while alloys are promising as PCMs, they are highly corrosive in their molten state and may react with structural materials. In our previous research, we developed a MEPCM with a Zn–30Al alloy core (melting point: 430–509 °C) and a three-layered coating comprising ZnO, $ZnAl_2O_4$, and γ-Al_2O_3 with about several-micrometer thickness, respectively.[135,136] The MEPCM was made by 2 steps; boehmite treatment in boiling water to form an aluminum hydroxide precursor coating on alloy particles and heat-oxidation treatment to obtain oxide coatings. The ZnO layer on the MEPCM surface acts as a semiconductor, offering potential for electrothermal conversion. This suggests that Zn–30Al MEPCM could also serve as an electric heater.

(3) Development of a composite PCM using MEPCM: our MEPCM can be handled like ceramic particles, allowing the development of composite PCMs. Previous studies demonstrated that a composite PCM with a cylindrical shape and a diameter of 1 cm could be prepared by manual mixing and sintering Zn–30Al MEPCM with glass frit (GF) as a sintering aid.[135,136] The composite PCM retained its shape even after 1000 solid–liquid thermal cycles.

Fig. 1 shows a schematic of the HSH using Zn–30Al MEPCM. The composite PCM shows potential as a HSH, due to its LHS capability from Zn–30Al and its suitable electrical resistivity for electrothermal conversion. This resistivity is achieved through percolation, forming a conducive network within the MEPCM. Notably, with the higher electrical resistivity design compared to existing electric heaters, the HSH is expected to be more suitable for ETES systems with high power input. Furthermore, because the composite PCM is fabricated using powder molding and sintering, the shape design is relatively flexible.[137,138] Therefore, it is possible to design better ETES systems with HSHs of various shapes that are compatible with the system and heat exchanger to be installed.

In the light of the foregoing, this study investigates the use of a composite PCM based on Zn–30Al MEPCM as a HSH. The morphology and properties of the composite PCM were analyzed. Additionally, electrothermal conversion capability and LHS performance were validated. These findings address the significant engineering challenge of incorporating large-scale electric heaters systems such as ETES, and they are expected to guide the design of innovative, integrated systems that

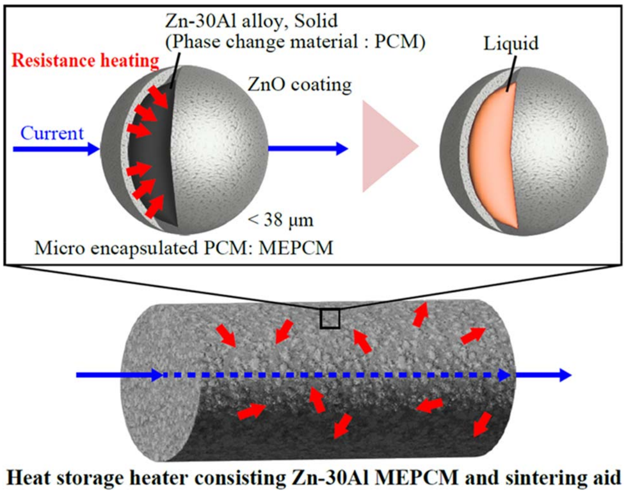

Fig. 1 Illustration of the HSH using Zn–30Al MEPCM.

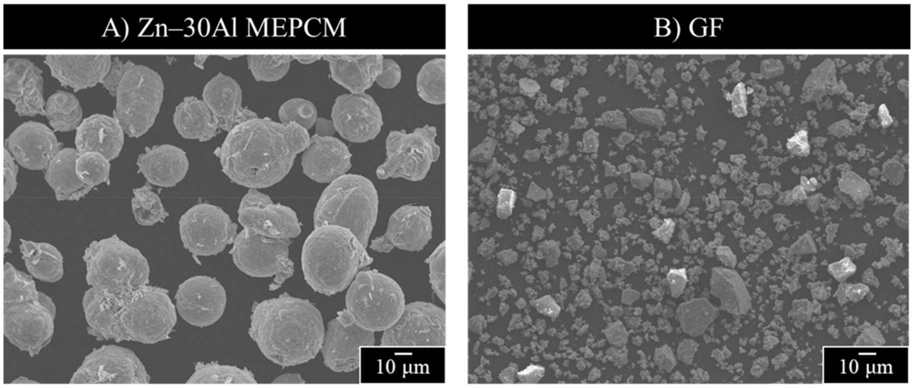

Fig. 2 SEM images of the (A) Zn–30Al MEPCM and (B) GF. These particles were used for making the HSH.

combine heaters and TESs. Therefore, the development of this HSH concept is poised to accelerate the implementation of ETES and further advance electrothermal conversion technologies.

Experimental

The fabrication of the Zn–30Al MEPCM and the composite PCM followed methods established in previous studies.[135,136] Subsequently, composite PCMs were prepared by mixing and sintering the Zn–30Al MEPCM with GF.

Raw materials

Zn–30Al alloy spherical particles (average diameter: 35.7 µm, purity: 99.0%) were sourced from Hikari Material Industry Co., Ltd. as the base material of the MEPCM. $Al(OH)_3$ powder (average diameter: 2.9 µm, purity: 99.99%), obtained from Kojundo Chemical Laboratory Co., Ltd., was incorporated into boehmite and precipitation treatment solutions to increase the amount of the precursor coating formed.

The GF (DSG006-S6, AGC Inc.), used as the sintering aid, had an average diameter of 14.6 µm, a density of 3.9448 g cm^{-3} (measured using an Ultrapycnometer 1000, Quantachrome Instruments), a glass transition temperature of 610 °C, and a softening point of 705 °C. Its primary constituents included ZnO, La_2O_3, B_2O_3, and MgO, with trace amounts of SiO_2, Al_2O_3, and BaO. Fig. 2 shows the scanning electron microscopy (SEM) images of the MEPCM and GF.

Preparation of MEPCM

Zn–30Al alloy particles were added to boiling water (300 mL) containing suspended $Al(OH)_3$ at a concentration of 1.7 g L^{-1}, achieving a particle concentration of 167 g L^{-1}. The mixture was stirred at 500 rpm for 3 hours to perform the boehmite treatment. Afterward, this treatment solution was cooled to 75 °C and left for 16 hours for the precipitation treatment. These processes formed a precursor coating of $Al(OH)_3$ and AlOOH on the alloy particles. After drying at 100 °C for 18 h, the samples of the precursor, weighing 5 g each, were placed in an alumina boat within an electric furnace under oxygen flow. The temperature was gradually increased to 800 °C at a rate of 10 °C min^{-1}, held for 3 hours, and cooled at the rate of 50 °C min^{-1} to 25 °C. The resulting MEPCM had a density of 4.3194 g cm^{-3}, measured using the pycnometer.

Preparation of composite PCM

To evaluate the impact of MEPCM content on sample properties relevant to the HSH, mixed powders with varying MEPCM proportions (25, 30, 40, 50, 60, 70, 75, and 80 vol% of the total volume) and GF were prepared. The powders were manually mixed by shaking them in a resealable plastic bag for 15 min.

A total of 0.5 or 2.5 g of the mixed powders was pressed at 20 MPa for 1 minute using a die with a diameter of 1 cm. The resulting green composite PCMs were heated to 800 °C at a rate of 5 °C min^{-1}, held at this temperature for 1 hour, and cooled to 25 °C at the same rate in air. The composite PCMs were labeled as ME*x*, where *x* corresponds to the MEPCM volume percentage

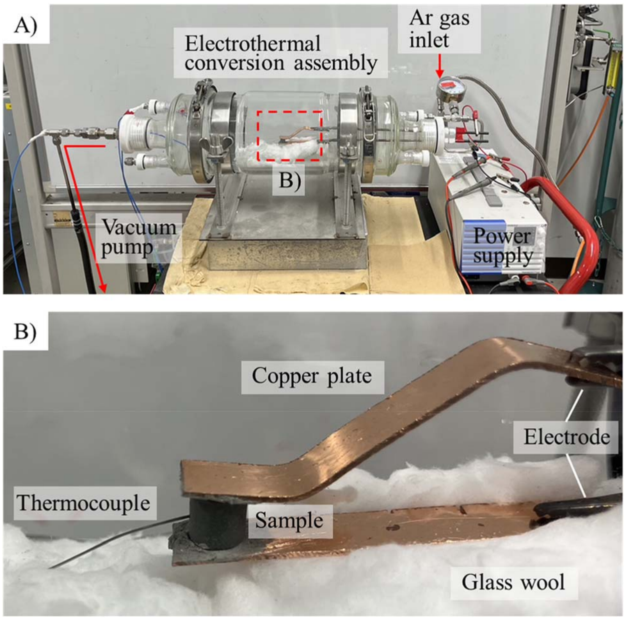

Fig. 3 (A) Setup and (B) enlarged view of the apparatus for electrical heating of the HSH. Panel (B) provides a close-up of the area highlighted with red dashed lines in (A).

(25, 30, 40, 50, 60, 70, 75, and 80 vol%) in the starting powder. Furthermore, the samples of 0.5 g and 2.5 g were used for sample analysis and electrical heating, respectively.

Characterization

The morphology and properties of the prepared composite PCM were analyzed. Their phases were identified through X-ray diffraction (XRD, Miniflex600, D/teX Ultra2, Cu Kα, $\lambda = 1.5418$ Å, Rigaku). Measurements were performed at a rate of 5° min^{-1} over a range of 3° to 90°. Cross-sections of the composite PCM were prepared using a cross-section polisher (IB-09010CP, JEOL) at the operation voltage of 6 kV. Field emission SEM (FE-SEM, JSM-7001FA, JEOL) and energy dispersive spectroscopy (EDX) were performed to observe the cross sections. Additionally, Auger electron spectroscopy (AES, JAMP-9500F, JEOL) provided a more detailed elemental analysis of the composite PCM cross-sections.

Bulk density, encompassing both open and closed pores, was determined using caliper (CD-15C, Mitutoyo) measurements to calculate the volume. The instrument error of the caliper are ±0.02 mm. Apparent density, which considers only closed pores, was measured using the pycnometer. Density measurements were performed five times for each composite PCM and the average of four readings, excluding the highest value, was taken as the apparent density. In addition, a calculated density was derived from the density and content of each material constituting the composite PCMs, defining an ideal density. The proportions of closed and open pores in the composite PCM were determined using the following equations:

$$\text{Closed pore }(\%) = 100 - \frac{\rho_A}{\rho_C} \times 100 \qquad (1)$$

$$\text{Open pore }(\%) = 100 - \frac{\rho_B}{\rho_C} \times 100 - \text{closed pore} \qquad (2)$$

where ρ_A, ρ_B, and ρ_C are the apparent, bulk, and calculated densities of the composite PCM samples, respectively.

The latent heat capacity and heat storage temperature of the composite PCM samples were measured through thermogravimetric analysis and differential scanning calorimetry (TGA-DSC, TGA-DSC-3, Mettler Toledo). The powder obtained from crushed composite PCM samples was added to an α-Al_2O_3 pan (30 μL) and heated and cooled from 100 to 600 °C at 5 °C min^{-1} in an airflow of 50 mL min^{-1}.

The volume resistivity of the composite PCM samples was investigated using a four-probe resistivity meter (Loresta-GP MCP-T610, Mitsubishi Chemical Analytech Co., Ltd). The terminals of the resistivity meter were brought into contact with each end of the composite PCM samples, and five measurements were taken per sample. This process was repeated for three samples under each condition and the average value was used to determine the electrical resistivity.

Electrical heating of composite PCM

To validate the electrothermal conversion and heat storage capabilities of the composite PCM, an electric current was applied. Fig. 3 shows the apparatus used for energizing the composite PCM samples. The ME50 sample was placed between copper plates connected to electrodes inside a quartz glass tube. These electrodes extended outside and were connected to a power supply (PWR801H, Kikusui Electronics).

For temperature measurement, a 1 mm diameter hole was drilled into the composite PCM, and a thermocouple was inserted. The recorded temperature corresponded to that at the center of the composite PCM. To minimize contact resistance, silver paste was applied between the composite PCM and copper plates. The quartz tube was evacuated with a vacuum pump after being purged five times with argon. The sample was

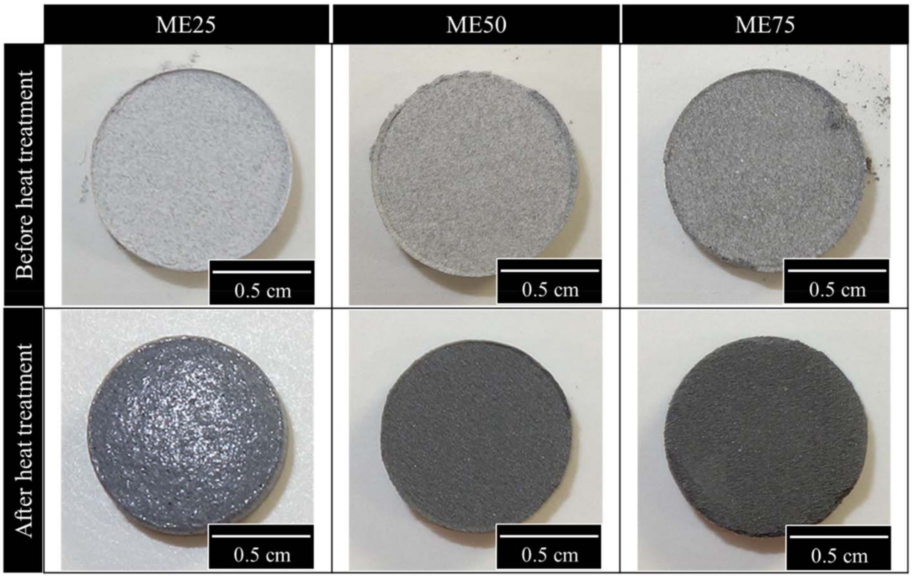

Fig. 4 Photographs of ME25, ME50, and ME75 before and after heat treatment.

then heated to 590 °C and held for 5 minutes to sinter the silver paste.

The electric power required to heat the sample to 590 °C was determined. Using this predefined current, the composite PCM was subjected to thermal cycling tests, by heating it to 590 °C and holding it for 1 minute before deactivating the power supply to allow cooling to 150 °C. These temperatures were chosen to achieve the phase changes of the alloy within the composite PCM. This heating and cooling cycle was repeated 10 and 100 times. Here, the cycling test of 100 times was performed in three separate stages consisting of 30, 30, and 40 cycles, respectively. Notably, previous studies have demonstrated that this composite PCM possesses high thermal cyclic durability, withstanding more than 1000 melting-solidification cycles when subjected to thermal cycling in an electric furnace.[136]

Results

Morphology of composite PCM

The results focus on ME25, ME50, and ME75, as the electrical resistivity trends of the composite PCM were categorized into three distinct classifications. Fig. 4 shows the photographs of the composite PCM before and after heat treatment, showing that their cylindrical shapes were retained. In contrast to the other samples, ME25 exhibited a shiny surface after heat treatment, attributed to its high GF content.

Fig. 5 shows the XRD patterns of ME25, ME50, ME75, and pure GF after heat treatment. The GF diffractogram shows multiple peaks attributable to its constituent oxides. In contrast, the XRD patterns of ME25, ME50, and ME75 patterns include additional peaks, confirming the presence of Al and Zn. The intensities of these Al and Zn peaks increase proportionally with the MEPCM content, reflecting the contribution of Zn–30Al PCM in the composite PCMs. These findings confirm the retention of the Zn–30Al alloy in the MEPCM after heat treatment.

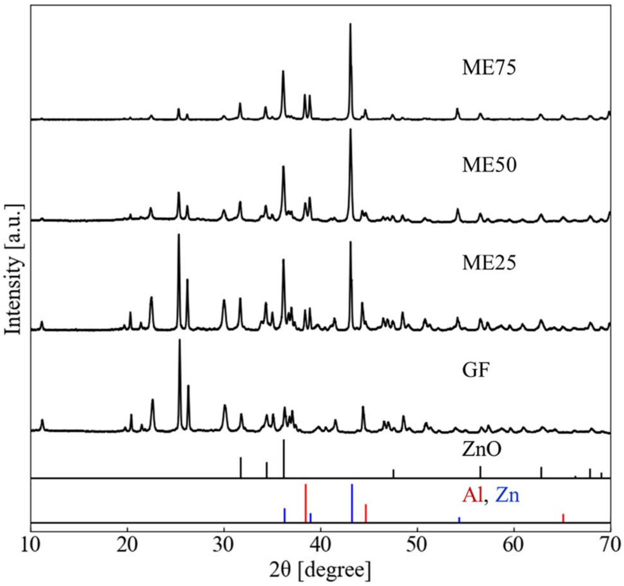

Fig. 5 Normalized XRD patterns of ME25, ME50, ME75, and GF after heat treatment, with reference peaks for Zn, Al, and ZnO displayed at the bottom.

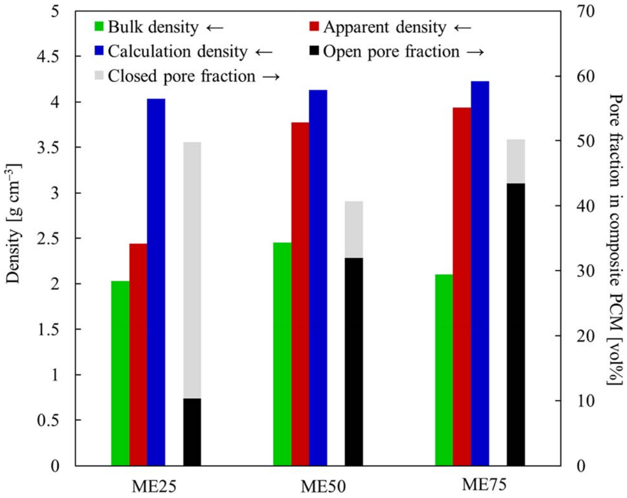

Fig. 6 Bulk density, apparent density, and calculation density of ME25, ME50, and ME75. Open and closed pore volume fractions are calculated from densities.

Fig. 6 shows the densities and pore volume fractions of ME25, ME50, and ME75. Among the three samples, ME50 exhibits the highest bulk density. Their apparent density increases with increasing MEPCM content. However, the bulk and apparent density are lower than their calculated density. This discrepancy confirms the presence of open and closed pores in the composite PCM. The open and closed pore volume fractions calculated from the densities decrease and increase, respectively, with increasing MEPCM content. Notably, the total pore volume fraction of ME50 is approximately 10% lower than those of ME25 and ME75.

Fig. 7 shows the SEM images and EDX elemental mappings of the cross sections of the as-prepared composite PCM. The cross-sectional images reveal circular grains 30 μm in diameter embedded within the matrix. The area occupied by the circular grains increases with increasing MEPCM content.

The EDX elemental mapping results confirm that the circular grains primarily contain Al and Zn, whereas the matrix contains most of O. From the shape of each phase and the detected elements, the circular and matrix phases were identified as the MEPCM and GF, respectively. This indicates that the spherical shape of the MEPCM particles was retained after the preparation of the composite PCM. In addition, the areas of the EDX map where no elements were detected represent the pores in the composite PCM. In particular, ME75 exhibited numerous pores.

Additionally, the regions in the EDX map where no elements were detected represent the pores within the composite PCM. Nearly circular shaped pores were observed in ME25, and irregularly shaped pores were confirmed along the MEPCM in ME50 and ME75.

Fig. 8 shows the Auger elemental mapping of the interface between the MEPCM and GF in ME50. A half-circular domain,

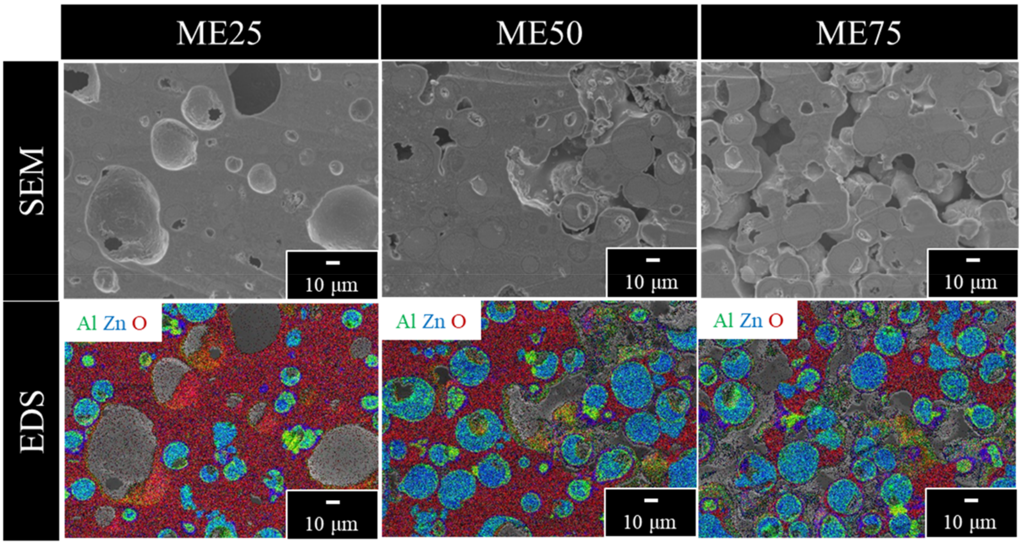

Fig. 7 SEM images and EDX elemental mapping of the cross-sections of the as-prepared HSHs.

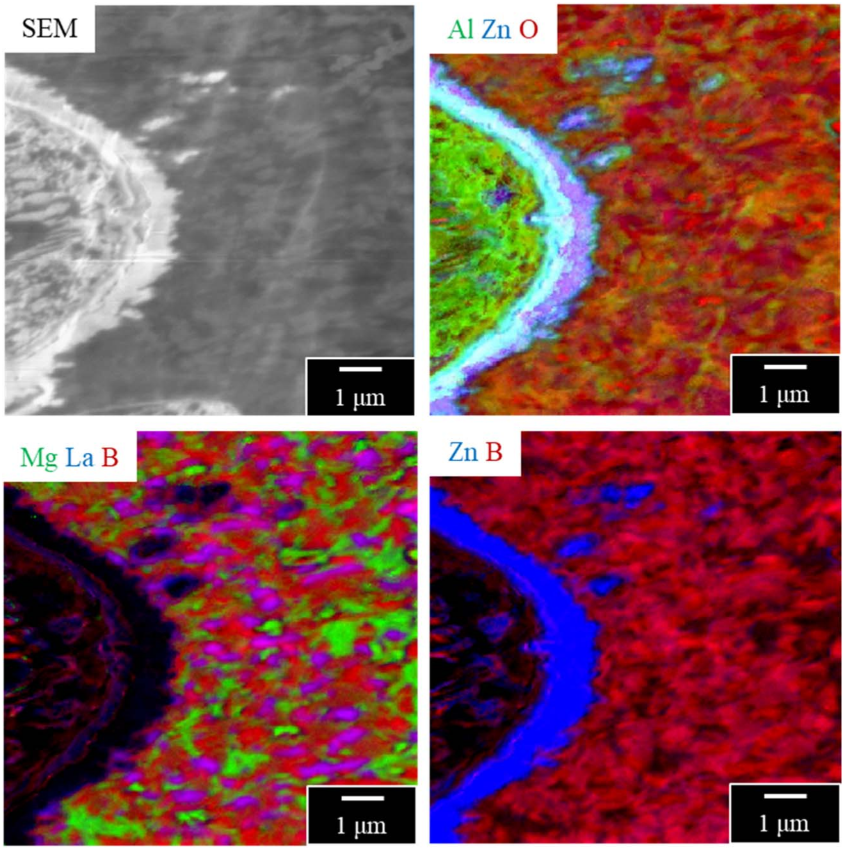

Fig. 8 Auger elemental mapping of the ME50 cross-section.

observed in the SEM image and corresponding to the MEPCM, contained Al and Zn. The surrounding matrix, identified as GF, is characterized by the presence of O. Additionally, B was distributed throughout the matrix, while Mg and La were localized within the GF phase. Mg and La act as the modification of the network structure of the glass frit.[139,140]

Electrothermal conversion in composite PCM

Fig. 9 shows the electrical resistivity of the composite PCM samples as a function of MEPCM content. In addition, due to the small range of variation across many conditions, the visibility of the error bars on Fig. 9 is limited. Therefore, the standard deviations for each condition are provided in Table

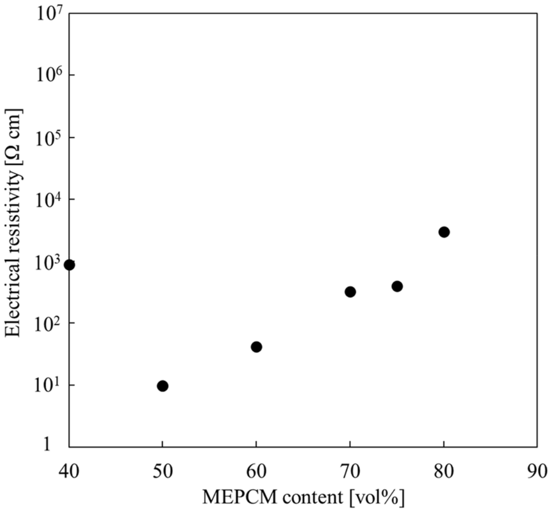

Fig. 9 Electric resistivity of the composite PCM as a function of MEPCM content. Resistivity measurements for GF, ME25, and ME30 are not reported because they exceeded the apparatus's upper limit of 10^7 Ω cm.

S2.† The resistivity of ME30, ME25, and GF exceeded the measurement limit of the apparatus (>10^7 Ω cm), categorizing these samples as insulators. The electrical resistivity of the composite PCMs decreased from ME30 to ME50 and then increased to ME80. Overall, the composite PCM samples exhibit sufficiently low resistivity to permit current flow. Furthermore, the electrical resistivity of the composite PCMs can be tuned by adjusting the MEPCM content, enabling tunability for various electrothermal conversion systems.

Fig. 10 illustrates the temperature profile of ME50 during 10 energization cycles. ME50 was selected for its ability to reach temperatures exceeding the PCM melting point, within the maximum voltage and current limits of the power supply used. Repeated cycles of heating and cooling (10 in total) were performed on ME50, consistently achieving the 590 °C target through electrical heating. Notably, temperature plateaus appeared at approximately 470 °C and 220 °C during the cooling phase, as shown in Fig. 10B and C. These plateaus correspond to solid–liquid and solid–solid phase transitions of the Zn–Al alloy, respectively, in accordance with the Zn–Al alloy phase diagram (Fig. S2†).

The difference between the phase change temperatures in the phase diagram and the observed plateaus in Fig. 10B and C was attributed to the undercooling of the Zn–30Al PCM. These findings confirm that ME50 demonstrates electrical heating and LHS, making it suitable for use as an HSH.

Fig. 11 shows the temperature profiles of ME50 during 100 cycles. The heating above the melting temperature of Zn–30Al

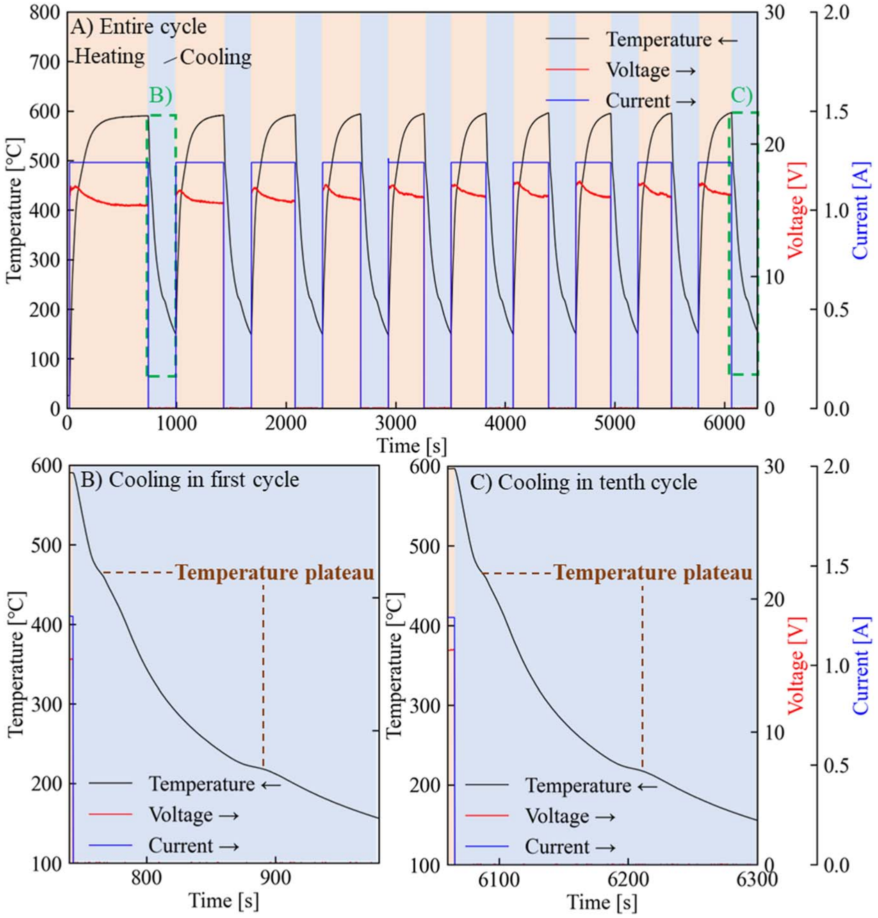

Fig. 10 Temperature variations of ME50 during energization, showing (A) the entire cycle and (B and C) the cooling phases of the first and tenth cycles, respectively. The regions marked with green dashed lines in (A) correspond to (B) and (C).

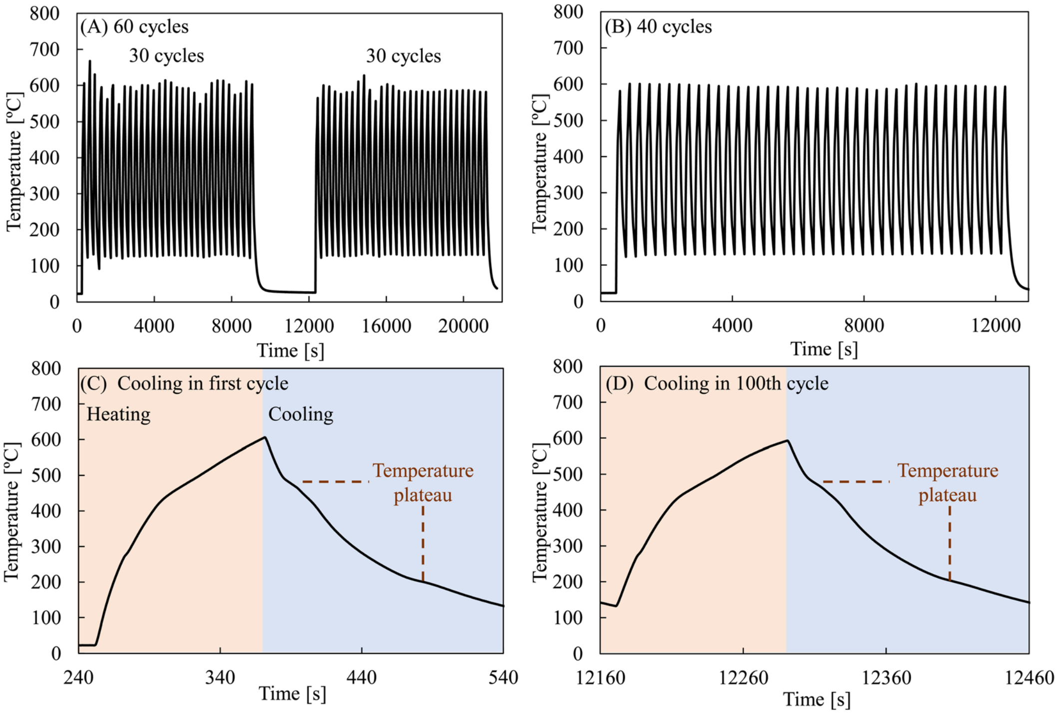

Fig. 11 Temperature profiles of ME50 during 100 cycles, showing (A) 60 cycles and (B) 40 cycles. By the combinations of the cyclic tests of (A) and (B), 100 cycles were performed. (C) and (D) The cooling phases of the first and 100th cycles from (A) and (B), respectively. By the combination cyclic tests of (A) and (B), 100 cycles were performed.

PCM was performed during the 100 cycles. The temperature plateau was observed from the profile during the cooling of 100 cycles. This result means that the resistance heating and the latent heat of ME50 keep after 100 cycles. Fig. 12 illustrates the SEM image and EDS mappings of the HSH surface. The particles with 20 μm-diameters were observed on the HSH surface. Zn and O were strongly detected on the particles. These particles correspond to the MEPCM as the raw materials of the HSH. SEM images and EDS mapping showed that the MEPCM on the surface of HSH retained its morphology and composition after 100 cycles.

Thermal properties of HSH

Fig. 13 shows the DSC heating curves of ME50 before and after 10 heating cycles. During heating, two endothermic peaks were observed; one at 280 °C and another within the 432–508 °C range, based on their onset and the onset-to-endset temperatures, respectively. Based on the Zn–Al alloy phase diagram (Fig. S2†), these peaks stem from the solid–solid and solid–liquid phase changes of the Zn–30Al alloy. The integral values of these peaks corresponded to the latent heat capacities of ME50, calculated as 15 J g^{-1} at 280 °C and 43 J g^{-1} at 432–508 °C. During cooling, exothermic peaks were confirmed at 248 °C (16 J g^{-1}) and within the 422–494 °C range (48 J g^{-1}). The downward temperature shift of these peaks compared to those during the heating phase reflects the supercooling of Zn–30Al. Importantly, the latent heat capacities and phase change temperatures remained consistent after 10 heating–cooling cycles, as depicted in Fig. 12B.

Fig. 14 shows the retention rate of the latent heat capacity of ME50 before and after cyclic tests. The latent heat capacities of 10 and 100 cyclic-tested ME50 retained 98% and 96% of that of the as-prepared HSH.

Table 1 presents the melting temperatures and latent heat capacities of the other HSHs obtained from TG-DSC results. The

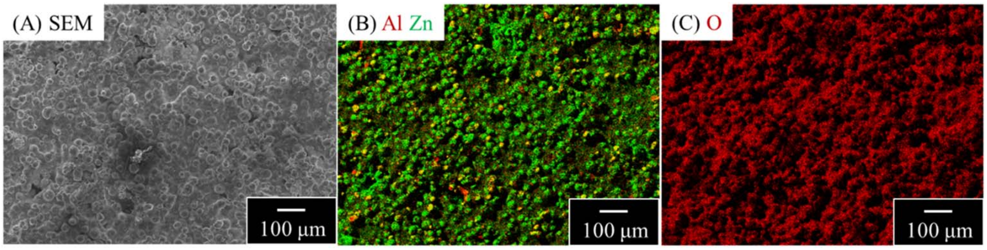

Fig. 12 (A) SEM images and EDS mappings of (B) Al, Zn, and (C) O illustrate the morphology of MEPCM on the HSH surface.

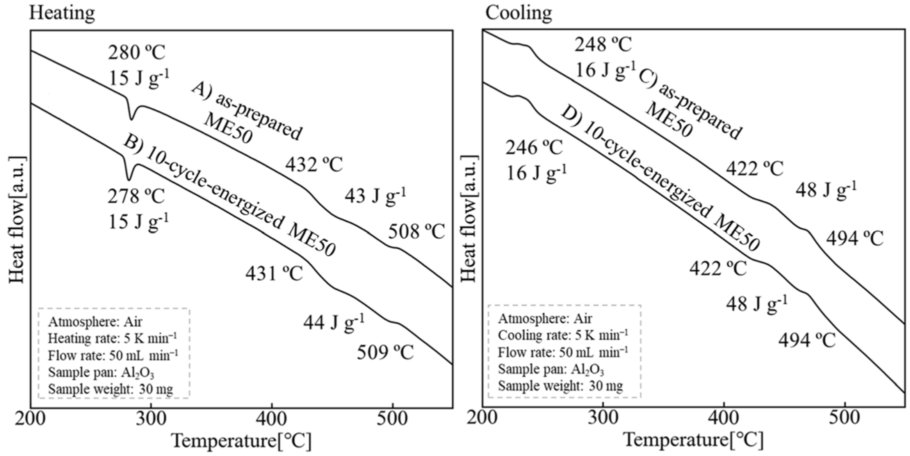

Fig. 13 DSC curves depicting (A and C) as-prepared and (B and D) 10 cycle-energized ME50 during heating and cooling.

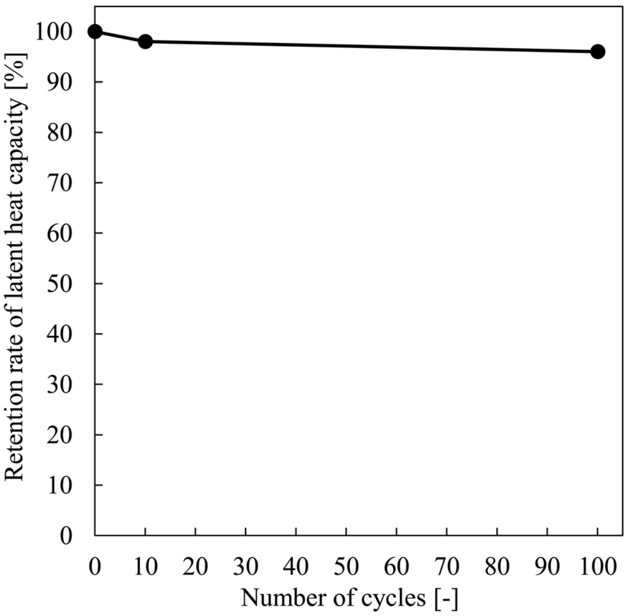

Fig. 14 Retention rate of latent heat capacity of ME50 before and after the cyclic tests. Latent heat capacities are based on the solid–liquid phase change of Zn–30Al during heating.

corresponding DSC curves for the MEPCM and HSHs except ME50 used to determine the melting temperatures and latent heat capacities are presented in Fig. S3.† The melting and solidification temperatures of all HSHs were similar to those of the Zn–30Al MEPCM. Additionally, the latent heat capacities of the HSHs increased proportionally with the MEPCM content.

Discussion

Electrical conduction mechanism of HSH

The electrical resistivity trends of the HSHs shown in Fig. 9, aligns similar with the percolation theory for conductive particles.[141] According to this theory, introducing filler materials with low electrical resistivity decreases the overall resistivity of a composite material. However, this relationship is nonlinear as it depends on the formation of a continuous conductive network by the filler material within the matrix. A sharp decrease in the electrical resistivity of a composite material occurs when the filler content exceeds a critical threshold. In this study, while GF, ME25, and ME30 exhibited high electrical resistivity, the electrical resistivity decreased from ME40 to ME50 due to the formation of a conductive network by the MEPCM filler material within the HSH.

Table 1 Melting and solidification temperatures (onset–endset) and calculated latent heat capacities derived from the DSC curves of the MEPCM and HSHs

	Heating		Cooling	
Sample name	Melting temperature [°C]	Latent heat capacity [J g^{-1}]	Melting temperature [°C]	Latent heat capacity [J g^{-1}]
Zn–30Al MEPCM (raw material of HSH)	438–512	85	425–499	90
ME40	433–516	35	425–497	45
ME50	432–508	43	422–494	48
ME60	435–510	51	421–491	63
ME70	436–511	59	423–492	65
ME75	437–513	61	422–494	68
ME80	437–513	64	425–499	73

In general, the percolation theory suggests that after a significant decrease, the electrical resistivity remains unchanged or decreases slowly as the filler material content increases. However, the resistivity of the HSHs increased with the MEPCM content beyond ME50, indicating that factors beyond percolation theory may influence this trend. Specifically, the shrinkage of GF due to softening and sintering during heat treatment may result in the rearrangement of the MEPCM within the HSH. The rearrangement generally increases the density of the HSHs. The softening and sintering effects of GF become more pronounced with increasing GF content. Despite this, as shown in Fig. 6, the pore volume fraction in ME50 was lower than in ME25, potentially due to inadequate mixing of the MEPCM and GF, which may have resulted in uneven sintering of particles. Improved mixing techniques could help achieve a more uniform distribution, aligning the electrical resistivity trends more closely with the predictions of percolation theory.

Comparison between typical electric heater and the HSH

Table 2 compares the electrical resistivity of typical electric heaters with that of the HSH.[142–145] The HSH exhibits higher electrical resistivity than conventional electric heaters, which offers a potential advantage in electrothermal conversion when using VRE.

During power transmission, electric power is typically reduced in voltage from several hundred kilovolts to a few hundred volts for end use applications.[146–148] In the case of conventional electric heaters, large current flow at these voltages, necessitates larger heater sizes, increasing both cost and spatial requirements. In contrast, the higher electrical resistivity of the HSH enables its potential application at higher voltages prior to transformation and has potential application about the reduction of the costs and energy losses associated with voltage transformation and save space. Future studies should investigate the HSH's voltage tolerance to establish its upper operational limits and assess its viability in such systems.

Interfacial reactions between MEPCM and GF

The HSHs were prepared by sintering GF and the MEPCM. During the heat treatment, GF softened and deformed to cover the MEPCM, as shown in Fig. 7 and 8. Additionally, interfacial reactions between the MEPCM shell and GF are expected at the interface of the two. In particular, B_2O_3, a primary component of GF (Fig. 8), can readily react with the ZnO coating of the MEPCM during the 800 °C heat treatment used for composite PCM preparation. Cedillo *et al.*[149] reported the synthesis of ZnB_2O_4 from ZnO and B_2O_3 at temperatures above 600 °C. While XRD, SEM-EDX, and AES results of the study (Fig. 5, 7 and 8, respectively) did not explicitly confirm the formation of oxides containing Zn and B, it may have formed in small regions at the interface between the MEPCM coating and GF. Such a reaction is hypothesized to yield a robust interface capable of enhancing the cyclic durability of the composite PCM.

Table 2 Comparison of electrical resistivity between typical electric heaters and the HSH in this study

Material	Electrical resistivity (Ω cm)	References
Ni–Cr	1.331×10^{-4}	142
Fe–Cr–Al	1.39×10^{-4}	143
Pt–Rh	1.87×10^{-5}	143
Ta	13.15×10^{-6}	144
W	5.28×10^{-6}	144
Mo	5.34×10^{-6}	144
C (graphite)	1.000×10^{-3}	143
$MoSi_2$	4×10^{-5}	143
SiC	0.05–0.48	145
HSH	$9.8–3.0 \times 10^{3}$	This study

Conclusion

In this study, we developed an HSH capable of electrothermal conversion as well as LHS at high temperatures. This dual functionality was achieved by employing a MEPCM with a Zn–30Al core and a ZnO coating. The HSHs were prepared by sintering the MEPCM and GF particles at 800 °C for 1 hour in an air atmosphere after mixing and pressing. The resulting HSHs exhibited electrical resistivities of more than 9.8 Ω cm induced by the MEPCM network within the structure. The electrical resistivities of the HSHs varied with the MEPCM content, suggesting that the electrical resistivity of the HSH can be tuned.

The HSH successfully reached 590 °C above the melting temperature of Zn–30Al PCM (432–508 °C) through electrical heating. During cooling, a temperature plateau resulting from the solidification of the Zn–30Al PCM was observed. After 100 cycle-energized HSHs, 96% of the latent heat capacity of the HSH was retained. These findings demonstrate the HSH's potential for high temperature electrothermal conversion and LHS.

This study lays the groundwork for incorporating HSH units into advanced energy storage and electrochemical conversion architectures. Future investigations should target larger heat storage capacities, extended operating temperature ranges, and modular system designs that facilitate seamless integration of the HSH. By doing so, these novel HSH-based ETES systems can enhance the utility of VRE in industrial and other energy-intensive settings, thereby advancing sustainable power solutions.

Data availability

The authors declare that the data supporting the findings of this study are available within the paper and its ESI files.†

Author contributions

Takahiro Kawaguchi: data curation, investigation, writing. Yusuke Sato: data curation. Joshua Chidiebere Mba: investigation, writing – review & editing. Yuto Shimizu: investigation, writing – review & editing. Kaixin Dong: investigation, writing – review & editing. Melbert Jeem: data curation, investigation, writing – review & editing. Takahiro Nomura: investigation, funding acquisition, project administration, supervision, writing – review & editing.

Conflicts of interest

There are no coflicts to declare.

Acknowledgements

This work was partially supported by JSPS KAKENHI, Grant Numbers 22K18993, and Grant-in-Aid for JSPS Fellows, Grant Numbers JP23KJ0032. This work is also based on results obtained from a project, JPNP20005, subsidized by the New Energy and Industrial Technology Development Organization (NEDO). The work was conducted in Hokkaido University, supported by "Advanced Research Infrastructure for Materials and Nanotechnology in Japan (ARIM)" of the Ministry of Education, Culture, Sports, Science and Technology (MEXT).

References

1 A. A. Kebede, T. Kalogiannis, J. Van Mierlo and M. Berecibar, *Renewable Sustainable Energy Rev.*, 2022, **159**, 112213.
2 IEA, *Net Zero by 2050 A Roadmap for the Global Energy Sector*, IEA, 2021.
3 LDES Council, *FLAGSHIP 2021 NET-ZERO POWER REPORT*, LDES Council, 2021.
4 M. Sun, T. Liu, X. Wang, T. Liu, M. Li, G. Chen and D. Jiang, *Carbon Neutrality*, 2023, **2**, 12.
5 P. Davenport, Z. Ma, J. Schirck, W. Nation, A. Morris, X. Wang and M. Lambert, *Sol. Energy*, 2023, **262**, 111908.
6 A. Azzuni and C. Breyer, *Energy Procedia*, 2018, **155**, 237–258.
7 A. Vecchi, K. Knobloch, T. Liang, H. Kildahl, A. Sciacovelli, K. Engelbrecht, Y. Li and Y. Ding, *J. Energy Storage*, 2022, **55**, 105782.
8 E. Papadis and G. Tsatsaronis, *Energy*, 2020, **205**, 118025.
9 X. Yu, H. Qiao, B. Yang and H. Zhang, *Energy Convers. Manage.*, 2023, **283**, 116959.
10 T. Neises and J. McTigue, *J. Eng. Gas Turbines Power*, 2025, **147**, 021008.
11 A. Basta, V. Basta, J. Spale, T. Dlouhy and V. Novotny, *J. Energy Storage*, 2022, **55**, 105548.
12 X. Zhang, Y. Sun, W. Zhao, C. Li, C. Xu, H. Sun, Q. Yang, X. Tian and D. Wang, *Energy Convers. Manage.*, 2023, **297**, 117724.
13 K. Johansen and S. Werner, *Renewable Sustainable Energy Rev.*, 2022, **158**, 112117.
14 H. Wang, X. Xue and C. Zhao, *Renewable Energy*, 2024, **228**, 120702.
15 V. Dreißigacker and G. Lucht, *Energies*, 2023, **16**, 7344.
16 R. Jacob and M. Liu, *Energies*, 2022, **16**, 189.
17 S. Tetteh, M. R. Yazdani and A. Santasalo-Aarnio, *J. Energy Storage*, 2021, **41**, 102829.
18 Y. Zhang, C. Zhang, Y. Wu, Y. Lu and Y. Lin, *J. Energy Storage*, 2024, **91**, 112143.
19 T. Melichar, K. Dočkal, O. Frýbort, P. Hájek and R. Filip, *Thermal Design of Latent Heat Thermal Energy Storage Facility with Supercritical CO_2*, Universität Duisburg-Essen, 2021.
20 S. Tetteh, G. Juul, M. Järvinen and A. Santasalo-Aarnio, *J. Energy Storage*, 2024, **86**, 111350.
21 M. Pecchini, S. Peccolo, A. Benato, F. De Vanna and A. Stoppato, *J. Energy Storage*, 2024, **100**, 113518.
22 W. Hu, R. Sun, K. Zhang, M. Liu and J. Yan, *J. Energy Storage*, 2023, **72**, 108698.
23 C. Xu, J. Pang, Y. Wu, T. Xin, J. Zhang and X. Xi, *J. Energy Storage*, 2023, **59**, 106328.
24 A. Alemam, N. L. Ferber, V. Eveloy, M. Martins, T. Malm, M. Chiesa and N. Calvet, *J. Energy Storage*, 2024, **86**, 111241.
25 A. R. Sane, N. Semlal, R. Boulif, C. Toussaint, A. Germeau, A. Nzihou and D. P. Minh, *Sol. Energy*, 2024, **278**, 112799.
26 T. Okazaki, *Renewable Energy*, 2020, **151**, 563–574.
27 J. R. Eggers, M. von der Heyde, S. H. Thaele, H. Niemeyer and T. Borowitz, *J. Energy Storage*, 2022, **55**, 105780.
28 J. Parham, P. Vrettos and N. Levinson, in *Ultra-High Temperature Thermal Energy Storage, Transfer and Conversion*, Elsevier, 2021, pp. 331–346.
29 M. Liu, W. Saman and F. Bruno, *Renewable Sustainable Energy Rev.*, 2012, **16**, 2118–2132.
30 L. Chen, R. Zou, W. Xia, Z. Liu, Y. Shang, J. Zhu, Y. Wang, J. Lin, D. Xia and A. Cao, *ACS Nano*, 2012, **6**, 10884–10892.
31 G. Wang, Z. Tang, Y. Gao, P. Liu, Y. Li, A. Li and X. Chen, *Chem. Rev.*, 2023, **123**, 6953–7024.
32 R. Cao, S. Chen, Y. Wang, N. Han, H. Liu and X. Zhang, *Carbon*, 2019, **149**, 263–272.
33 W. Aftab, A. Mahmood, W. Guo, M. Yousaf, H. Tabassum, X. Huang, Z. Liang, A. Cao and R. Zou, *Energy Storage Mater.*, 2019, **20**, 401–409.
34 Q. Sun, N. Zhang, H. Zhang, X. Yu, Y. Ding and Y. Yuan, *Renewable Energy*, 2020, **145**, 2629–2636.
35 Z. Zheng, J. Jin, G.-K. Xu, J. Zou, U. Wais, A. Beckett, T. Heil, S. Higgins, L. Guan and Y. Wang, *ACS Nano*, 2016, **10**, 4695–4703.
36 M. Du, C. Guo, Y. Cai, J. Liu, Q. Wei and L. Li, *J. Energy Storage*, 2021, **43**, 103187.
37 X. Guo, C. Liu, N. Li, S. Zhang and Z. Wang, *Ind. Eng. Chem. Res.*, 2018, **57**, 15697–15702.
38 Z. Liu, R. Zou, Z. Lin, X. Gui, R. Chen, J. Lin, Y. Shang and A. Cao, *Nano Lett.*, 2013, **13**, 4028–4035.
39 T. Li, M. Wu, S. Wu, S. Xiang, J. Xu, J. Chao, T. Yan, T. Deng and R. Wang, *Nano Energy*, 2021, **89**, 106338.
40 C. Li, B. Zhang and Q. Liu, *J. Energy Storage*, 2020, **29**, 101339.
41 H. Tabassum, X. Huang, R. Chen and R. Zou, *J. Materiomics*, 2015, **1**, 229–235.
42 G. Li, Y. Wang and X. Zhang, *FlatChem*, 2021, **27**, 100249.
43 G. Yang, L. Zhao, C. Shen, Z. Mao, H. Xu, X. Feng, B. Wang and X. Sui, *Sol. Energy Mater. Sol. Cells*, 2020, **209**, 110441.
44 A. Li, C. Dong, H. Gao, X. Chen, Y. Tang and G. Wang, *Renewable Energy*, 2021, **170**, 661–668.
45 H. Wu, S. Deng, Y. Shao, J. Yang, X. Qi and Y. Wang, *ACS Appl. Mater. Interfaces*, 2019, **11**, 46851–46863.

46 W. Wu, X. Huang, K. Li, R. Yao, R. Chen and R. Zou, *Appl. Energy*, 2017, **190**, 474–480.
47 C. Dong, A. Li, C. Wang, J. Li, H. Gao, X. Chen, Y. Wang, L. Li, Y. Zheng and G. Wang, *Chem. Eng. J.*, 2022, **430**, 133007.
48 D. Huang, Z. Wang, X. Sheng and Y. Chen, *Sol. Energy Mater. Sol. Cells*, 2023, **251**, 112124.
49 X. Lu, H. Huang, X. Zhang, P. Lin, J. Huang, X. Sheng, L. Zhang and J.-p. Qu, *Composites, Part B*, 2019, **177**, 107372.
50 A. Li, C. Dong, W. Dong, F. Yuan, H. Gao, X. Chen, X. B. Chen and G. Wang, *Adv. Electron. Mater.*, 2020, **6**, 1901428.
51 Y. Zhou, X. Wang, X. Liu, D. Sheng, F. Ji, L. Dong, S. Xu, H. Wu and Y. Yang, *Carbon*, 2019, **142**, 558–566.
52 Y. Li, Y. A. Samad, K. Polychronopoulou, S. M. Alhassan and K. Liao, *J. Mater. Chem. A*, 2014, **2**, 7759–7765.
53 G. Li, X. Zhang, J. Wang and J. Fang, *J. Mater. Chem. A*, 2016, **4**, 17042–17049.
54 M. M. Umair, Y. Zhang, A. Tehrim, S. Zhang and B. Tang, *Ind. Eng. Chem. Res.*, 2020, **59**, 1393–1401.
55 H. Ji, D. P. Sellan, M. T. Pettes, X. Kong, J. Ji, L. Shi and R. S. Ruoff, *Energy Environ. Sci.*, 2014, **7**, 1185–1192.
56 R. Chen, R. Yao, W. Xia and R. Zou, *Appl. Energy*, 2015, **152**, 183–188.
57 L. Kong, Z. Wang, X. Kong, L. Wang, Z. Ji, X. Wang and X. Zhang, *ACS Appl. Mater. Interfaces*, 2021, **13**, 29965–29974.
58 M. M. Umair, Y. Zhang, S. Zhang, X. Jin and B. Tang, *J. Mater. Chem. A*, 2019, **7**, 26385–26392.
59 B. Xie, C. Li and Y.-L. He, *J. Energy Storage*, 2023, **59**, 106367.
60 H. Zhang, Q. Sun, Y. Yuan, Z. Zhang and X. Cao, *Chem. Eng. J.*, 2018, **336**, 342–351.
61 Z. Liu, B. Tang and S. Zhang, *Composites, Part A*, 2023, **166**, 107387.
62 Y.-y. Xiao, D.-y. Bai, Z.-p. Xie, Z.-y. Yang, J.-h. Yang, X.-d. Qi and Y. Wang, *Composites, Part A*, 2021, **146**, 106420.
63 Y. J. He, Y. W. Shao, Y. Y. Xiao, J. H. Yang, X. D. Qi and Y. Wang, *ACS Appl. Mater. Interfaces*, 2022, **14**, 6057–6070.
64 Y. Liu, H. Liu and H. Qi, *J. Colloid Interface Sci.*, 2023, **629**, 478–486.
65 J. Song, Y. Cai, M. Du, X. Hou, F. Huang and Q. Wei, *ACS Appl. Bio Mater.*, 2020, **3**, 8923–8932.
66 X. Liu, J. Miao, Q. Fan, W. Zhang, X. Zuo, M. Tian, S. Zhu, X. Zhang and L. Qu, *ACS Appl. Mater. Interfaces*, 2021, **13**, 56607–56619.
67 J. Zhao, J. Zhou, H. Li and A. Xiao, *Carbohydr. Polym.*, 2023, **316**, 121031.
68 J. Wu, M. Wang, L. Dong, J. Shi, M. Ohyama, Y. Kohsaka, C. Zhu and H. Morikawa, *ACS Nano*, 2022, **16**, 12801–12812.
69 Y. Yang, S. Liu, L. Jin, G. Li, B. Quan, Q. Chen, X. Tang, X. Ji, H. Wu and X. Lu, *Composites, Part A*, 2023, **175**, 107803.
70 Y.-C. Zhou, J. Yang, W.-D. Li, P. Yu, Z.-M. Zhang, L. Bai, R.-Y. Bao and W. Yang, *Chem. Eng. J.*, 2023, **470**, 144175.
71 Z. Hu, M. Jiang, Y. Zou, L. Sun, F. Xu, S. Yu, S. Hao and C. Xiang, *Chem. Eng. J.*, 2023, **461**, 141923.
72 M. Liu, X. Zhang, X. Liu, X. Wu, X. Ye, J. Qiao, Z. Sun, X. Zhu and Z. Huang, *ACS Sustain. Chem. Eng.*, 2022, **10**, 8051–8063.
73 S. Nishad, P. Kasak and I. Krupa, *J. Energy Storage*, 2023, **66**, 107449.
74 Z. Niu and W. Yuan, *ACS Appl. Mater. Interfaces*, 2021, **13**, 4508–4518.
75 Y. Ding, X. Lu, S. Liu, H. Wu, X. Sheng, X. Li and J. Qu, *Composites, Part A*, 2022, **163**, 107178.
76 X. Liu, F. Lin, G. Leng, M. Liu, J. Feng, Y. Bai, Z. Guo, Y. Xu, Z. Sun and Z. Huang, *J. Energy Storage*, 2023, **73**, 108959.
77 L. Yu, X. Qin, G. Ke, J. Tang and Y. Wang, *Compos. Commun.*, 2022, **32**, 101152.
78 R. Liu, A. Li, J. Liu, W. Liu, H. Zheng, Q. Du, X. Chen and C. Dong, *Chem. Eng. J.*, 2023, **474**, 145814.
79 G. Cheng, Z. Wang, X. Wang and Y. He, *Appl. Energy*, 2022, **322**, 119509.
80 M. Maleki, N. Sharifi, H. Karimian, R. Ahmadi, P. Aminizadeh, R. Sandgol and A. Valanezhad, *J. Energy Storage*, 2023, **67**, 107599.
81 Y. Cai, N. Zhang, X. Cao, Y. Yuan, Z. Zhang and N. Yu, *Sol. Energy Mater. Sol. Cells*, 2023, **252**, 112176.
82 X. Ye, L. Yang, Z. Tian, P. Zhou, S. Wang, H. Sun, Z. Zhu, J. Li, W. Liang and A. Li, *Sol. Energy Mater. Sol. Cells*, 2022, **245**, 111873.
83 L. Cheng, L. Kong, X. Zhang and X. Kong, *Sol. Energy Mater. Sol. Cells*, 2022, **235**, 111461.
84 X. Lin, Z. Ling, X. Fang and Z. Zhang, *Appl. Energy*, 2022, **327**, 120141.
85 B. Zhang, C. Li and Q. Liu, *Therm. Sci. Eng. Prog.*, 2021, **25**, 101039.
86 M. Wang, C. Zhang, J. Wang, Y. Wang and F. Yu, *J. Energy Storage*, 2022, **52**, 104905.
87 M. He, J. Lu, C. Shi, X. Qian, L. Yin, K. Gong and K. Zhou, *ACS Appl. Nano Mater.*, 2023, **6**, 16503–16514.
88 L. Yang, J. Yang, L.-S. Tang, C.-P. Feng, L. Bai, R.-Y. Bao, Z.-Y. Liu, M.-B. Yang and W. Yang, *Energy Fuels*, 2020, **34**, 2471–2479.
89 M. Y. Yazici, *Therm. Sci. Eng. Prog.*, 2022, **29**, 101244.
90 D. Huang, Y. Chen, L. Zhang and X. Sheng, *J. Mater. Sci. Technol.*, 2023, **165**, 27–38.
91 C. Yin, L. Weng, Z.-X. Fei, L.-Y. Shi and K.-K. Yang, *Chem. Eng. J.*, 2022, **431**, 134206.
92 S. Liu, B. Quan, Y. Yang, H. Wu, Q. Chen, G. Li, Z. Tao, C. Zhu, X. Lu and J. Qu, *J. Energy Storage*, 2023, **67**, 107592.
93 F. Lin, X. Liu, G. Leng, Y. Bai, J. Feng, Z. Guo, Z. Wang, Z. Huang, R. Mi and X. Min, *Carbon*, 2023, **201**, 1001–1010.
94 J.-F. Su, Y.-D. Guo, X.-M. Xie, X.-L. Zhang, R. Mu, Y.-Y. Wang and Y.-Q. Tan, *Constr. Build. Mater.*, 2019, **224**, 671–681.
95 S. Liu, B. Quan, M. Sheng, Y. Yang, X. Hu, C. Zhu, X. Lu and J. Qu, *Nano Energy*, 2023, **114**, 108669.
96 Y. Ma, N. Lu, Z. Hu, J. Zhang, X. Cao, J. Li, Z. Zhu, H. Sun, W. Liang and A. Li, *Sol. Energy Mater. Sol. Cells*, 2023, **250**, 112076.
97 X. Wei, X.-z. Jin, N. Zhang, X.-d. Qi, J.-h. Yang, Z.-w. Zhou and Y. Wang, *Carbohydr. Polym.*, 2021, **253**, 117290.

98 C. Pan, P. He, N. Chen, J. Wu, E. Shi, A. Wang, H. Jia, J. Wei and T. Hu, *J. Energy Storage*, 2023, **57**, 106225.

99 S. Hao, Y. Zou, C. Xiang, L. Sun, F. Xu and Z. Hu, *J. Energy Storage*, 2023, **72**, 108615.

100 G. Zhou, L. Li, S.-Y. Lee, F. Zhang, J. Xie, B. Ye, W. Geng, K. Xiao, J.-H. Lee and S.-J. Park, *Compos. Sci. Technol.*, 2023, **243**, 110256.

101 C. Liang, W. Zhang, C. Liu, J. He, Y. Xiang, M. Han, Z. Tong and Y. Liu, *Chem. Eng. J.*, 2023, **471**, 144500.

102 G. Ke, X. Jin, G. Cai, W. Li and A. Xu, *J. Ind. Text.*, 2022, **51**, 554S–568S.

103 X. Chen, J. Xu, Y. Li, Y. Gao and G. Wang, *SusMat*, 2023, **3**, 510–521.

104 M. Luo, J. Song, Z. Ling, Z. Zhang and X. Fang, *Mater. Today Energy*, 2021, **20**, 100652.

105 L. Chen, J. Lv, L. Ding, G. Yang, Z. Mao, B. Wang, X. Feng, S. Zapotoczny and X. Sui, *Chem. Eng. J.*, 2020, **400**, 125950.

106 H. He, Y. Wang, Z. Zhao, Q. Wang, Q. Wei and Y. Cai, *J. Energy Storage*, 2022, **55**, 105358.

107 J. Deng, Y. Kou, H. Liu, M. Yang, K. Sun, R. Joshi and Q. Shi, *ACS Appl. Energy Mater.*, 2023, **6**, 7457–7467.

108 Z. Wang, X. Zhang, X. Min and M. Fang, *J. Energy Storage*, 2022, **55**, 105854.

109 J. Lv, J. Wang, T. Zhang, B. Yang, Z. Zhen, Y. Zheng and Y. Wang, *J. Energy Storage*, 2023, **61**, 106771.

110 X. Zhu, J. Liu, K. Yang, L. Zhang, S. Wang and X. Liu, *Composites, Part B*, 2024, **272**, 111233.

111 L. Hu, J. Chen, J. She, F. Li, J. Liao, Y. Zhou and Y. Zhang, *J. Energy Storage*, 2024, **77**, 109802.

112 M. R. Y. McCord, A. Kankkunen, D. Chatzikosmidou, A. Seppälä, J. Seppälä and H. Baniasadi, *J. Energy Storage*, 2024, **81**, 110363.

113 M. Fan, Z. Luan, H. Li, X. Kong and Y. Kang, *Energy*, 2024, **294**, 130863.

114 J. Wang, W. Li and X. Zhang, *J. Mater. Sci. Technol.*, 2024, **178**, 179–187.

115 Q. Liang, H. Zhang, Y. Li, X. Zhang and D. Pan, *J. Energy Storage*, 2024, **83**, 110621.

116 L. Chen, L. Luo, Z. Mao, B. Wang, X. Feng and X. Sui, *ACS Appl. Mater. Interfaces*, 2024, **16**, 4089–4098.

117 J. Zhang, Z. Zheng, L. Xu, H. Xie, Z. Fei, P. J. Dyson and N. Yan, *Colloids Surf., A*, 2024, **690**, 133783.

118 T. Luo, L. Kong, L. Li, J. Lu, Z. Yu, B. Lin, L. Fu and C. Xu, *Chem. Eng. J.*, 2024, **486**, 150443.

119 J. Zuo, H. Luo, Z. Ling, Z. Zhang, X. Fang and W. Zhang, *Ind. Chem. Mater.*, 2024, **2**, 571–586.

120 Y. Li, H. Yu, P. Liu, X. Diao, Y. Feng, Y. Jiang and X. Chen, *SusMat*, 2024, e214.

121 Y. Zhao, P. Zhang, Y. Qiu, Q. Li, H. Yan, Z. Wang and C. Wu, *DeCarbon*, 2024, **5**, 100051.

122 J. Su, J. Lin, Y. Cao, W. Xu, M. Weng, J. Huang, H. Zhang and Y. Min, *Appl. Therm. Eng.*, 2024, **253**, 123774.

123 W. Luo, X. Hu, M. Zou, L. Luo, Y. Ma, W. Chen and X. Jiang, *J. Energy Storage*, 2024, **103**, 114373.

124 J. Wu, Y. Wang, P. Song, M. Sang, Z. Fan, Y. Xu, X. Wang, S. Liu, Z. Li and S. Xuan, *Nano Lett.*, 2024, **24**, 14020–14027.

125 Y. He, S. Guo, X. Zuo, M. Tian, X. Zhang, L. Qu and J. Miao, *ACS Appl. Mater. Interfaces*, 2024, **16**, 59358–59369.

126 M. Liu, S. Zhang, Y. Shi, Z. Fang, J. Wang and C. Bao, *Chem. Eng. J.*, 2024, **499**, 156509.

127 G. T. Nguyen, N. T. Thi, N. T. Nho and H. N. A. Tuan, *J. Sci.: Adv. Mater. Devices*, 2024, **9**, 100792.

128 Y. Jiang, X. Liu, F. Lin, Z. Guo, J. Qiao, J. Fan, Y. Liu, R. Mi, X. Min and Z. Huang, *Mater. Lett.*, 2024, **377**, 137385.

129 Z. Zhang, Y. He, H. Ma, X. Liu, Y. Zhou and Y. Yang, *Chem. Eng. Res. Des.*, 2024, **210**, 130–139.

130 D. Niu, T. Zhang, X. Zhang, Y. Tan and L. Zhai, *Energy Technol.*, 2024, **12**, 2400707.

131 R. Yan, Z. Huang, L. Zhang, Y. Chen and X. Sheng, *Compos. Commun.*, 2024, **51**, 102047.

132 Y. Ma, J. Shen, T. Li, X. Sheng and Y. Chen, *Sol. Energy Mater. Sol. Cells*, 2024, **276**, 113078.

133 R. Yan, Z. Huang, Y. Chen, L. Zhang and X. Sheng, *Int. J. Biol. Macromol.*, 2024, **277**, 134233.

134 X. Li, C. Ge, K. Chen, H. Guan and X. Zhang, *J. Energy Storage*, 2024, **102**, 114177.

135 T. Kawaguchi, H. Sakai, N. Sheng, A. Kurniawan and T. Nomura, *Appl. Energy*, 2020, **276**, 115487.

136 T. Kawaguchi, H. Sakai, R. Ishida, Y. Shimizu, A. Kurniawan and T. Nomura, *J. Energy Storage*, 2022, **55**, 105577.

137 H. Sakai, N. Sheng, A. Kurniawan, T. Akiyama and T. Nomura, *Appl. Energy*, 2020, **265**, 114673.

138 H. Koide, A. Kurniawan, T. Takahashi, T. Kawaguchi, H. Sakai, Y. Sato, J. N. W. Chiu and T. Nomura, *Energy*, 2022, **238**, 121746.

139 P. Lu, Y. Zheng, J. Cheng and D. Guo, *Ceram. Int.*, 2013, **39**, 8207–8212.

140 J. Choi and K. Kim, *J. Non-Cryst. Solids*, 2013, **646**, 123230.

141 C.-W. Nan, Y. Shen and J. Ma, *Annu. Rev. Mater. Res.*, 2010, **40**, 131–151.

142 T. Hüpf, C. Cagran, E. Kaschnitz and G. Pottlacher, *Thermochim. Acta*, 2009, **494**, 40–44.

143 A. Yavaş, *Carbon Based Heating Elements and Their Practical Applications*, Izmir Katip Celebi University, Turkey, 2019.

144 P. D. Desai, T. K. Chu, H. M. James and C. Y. Ho, *J. Phys. Chem. Ref. Data*, 1984, **13**, 1069–1096.

145 K. Pelissier, T. Chartier and J. Laurent, *Ceram. Int.*, 1998, **24**, 371–377.

146 H. I. Elsayed, A. Khadam and O. H. Elhassan, *Presented in Part at the 2019 International Conference on Computer, Control, Electrical, and Electronics Engineering (ICCCEEE)*, Khartoum, Sudan, September, 2019.

147 S. Yue, W. Ji, J. Xu, J. Zhang and S. Wang, *Presented in Part at the 2022 IEEE Sustainable Power and Energy Conference (iSPEC)*, Perth, Australia, December, 2022.

148 F. Molnár, *Interdiscip. Descr. Complex Syst.*, 2023, **21**, 161–167.

149 G. Cedillo, E. Cruz Z, M. Garcia H, J. Marcazzo, J. Hernandez A and H. Murrieta S, *Presented in Part at the International Symposium on Solid State Dosimetry (ISSSD)*, León, Guanajuato, Mexico, September, 2015.